Precipitation in an A356 foundry alloy with Cu additions - A Transmission Electron Microscopy Study

Eva A.Mørtsell[a], Feng Qian[a], Calin D. Marioara[b], Yanjun Li[a,*]

[a]*Department of Materials Science and Engineering, Norwegian University of Science and Technology (NTNU), Alfred Getz' veg 2, N-7491 Trondheim, Norway*
[b]*SINTEF Materials and Chemistry, N-7491 Trondheim, Norway*

Abstract

The influence of different Cu addition levels on the age hardening and precipitation behaviors in an Al356 foundry alloy during artificial aging treatments has been systematically studied. A detailed characterization of the precipitates at the atomic scale has been done by using high angle annular dark field (HAADF) scanning transmission electron microscopy (STEM). At peak hardness, the number density of needle shape precipitates increases with increasing Cu content, while the dominant hardening precipitates change from β'' in the Cu-free alloy to L and Q' phases in the Cu-added alloys. It is discovered that the cross section of a large fraction of L-phase contains an inversion centre, predominantly at the central Si atomic column in the lattice. It was also observed that some β'' precipitates incorporate Cu atoms at the Si_3-sites in the β''-molecule. In addition to the Mg-Si-(Cu) precipitates, a large fraction of nano-sized Si particles also precipitated in all the three alloys during artificial aging, which is attribute to the excess Si in solid solution.

Keywords: Aluminium, Foundry alloy, Silicon, Copper, TEM, Precipitates

1. Introduction

Al-Si-Mg based aluminium foundry alloys have very good casting properties partly due to the presence of the Al-Si eutectic phases causing high fluidity of the material. The foundry alloys are highly resistant to corrosion and

*Corresponding author: yanjun.li@ntnu.no.

have a high strength to weight ratio. More importantly, the strength of the alloys can be improved by age hardening treatments. This effect is mainly attributed to the precipitation of metastable precipitate phases, acting as dislocation impediments during deformation of the material [1, 2].These advantageous properties makes the materials highly suitable for cast structures where complex shapes and high strength are required, such as automotive components. Two of the most common foundry alloys are A356 and A357, which are usually produced from secondary aluminium alloys and have a Si content of about 7 wt%.

Different alloying elements can be added into the alloys to further improve their strength. Cu has been reported to improve the mechanical properties of Al-Si-Mg foundry alloys after age-hardening, such as strength and hardness [2]. An addition of 3 wt% Cu could lead to the precipitation of θ' phases. Zr[3] and Hf [4] were also added to the alloys to improve the elevated temperature strength of the alloys. An addition of Hf resulted in formation of Hf nanobelts, which can improve ductility significantly without making any sacrifice in material strength [4].

Characterization of the age hardening precipitates down to the atomic scale has become increasingly important for development of alloy systems. As it is commonly accepted that needle shaped precipitate structures formed during heat treatment contribute significantly to the macroscopic properties of the alloys, a detailed understanding of these structures is important in order to tailor specialized materials.

The precipitation sequence in 6xxx Al-Mg-Si alloys has been widely studied, and is in general given as follows: [5, 6]

$$\begin{aligned} \text{SSSS} &\Rightarrow \text{Atomic clusters [7–9]} \Rightarrow \text{GP-zones [10]} \\ &\Rightarrow \beta''[11, 12] \Rightarrow \beta'[13, 14], \text{U1}[15], \text{U2}[16], \text{B}'[17] \Rightarrow \beta[18,\ 19], \text{Si}[20]. \end{aligned} \tag{1}$$

β'' is the main phase associated with peak hardness in Al-Mg-Si alloys. A summary of the known existing phases in 6xxx Al-Mg-Si alloys is given in Table 1.

By adding a small amount of Cu, other precipitate phases become dominant and the formation of β" is suppressed [22, 23]. The precipitation sequence with Cu-additions is given in Sequence 2.

Table 1: Precipitate phases encountered in 6xxx Al-Mg-Si alloys [21].

Phase	Composition	Space group	Lattice parameters [nm]
GP-zones	Variable	*C2/m*	a = 1.48, b = 0.405, c = 0.648, β = 105.3°
β"	$Mg_{6-x}Al_{1+x}Si_4$ ($0 \leqq x \leqq 2$)	*C2/m*	a = 1.516, b = 0.405, c = 0.674, β = 105.3°
β'	$Mg_{1.8}Si$	$P6_3/m$	a = b = 0.715, c = 0.405, γ = 120°
U1	$MgAl_2Si_2$	$P\bar{3}m1$	a = b = 0.405, c = 0.674, γ = 120°
U2	MgAlSi	*Pnma*	a = 0.675, b = 0.405, c = 0.794
B'	$Mg_9Al_3Si_7$	Hexagonal	a = b = 1.04, c = 0.405, γ = 120°
β	Mg_2Si	$Fm\bar{3}m$	a = 0.635

$$\begin{aligned} \text{SSSS} \Rightarrow \text{Atomic clusters [7–9]} \Rightarrow \text{GP-zones [10]} \\ \Rightarrow \beta''[11,\ 12], L[23], C[24], QP[25], QC[25] \\ \Rightarrow \beta'[13,\ 14], Q'[20,\ 22,\ 26] \Rightarrow Q[27,\ 28]. \end{aligned} \tag{2}$$

The main metastable phases in the Al-Mg-Si(-Cu) alloys are fully coherent with the Al matrix along $<100>_{\text{Al}}$. That is, they grow with needle/lath/rod or plate morphologies along these directions. It has been documented that the metastable phases are structurally connected by a network of Si atomic columns with hexagonal a = 0.4 nm projection along their needle directions, often referred to as the 'Si-network' [29, 30].

The L phase is lath shaped, elongated along $<001>_{\text{Al}}$ with a habit plane aligning along $<100>_{\text{Al}}$, and often displays a disordered structure [23, 31]. L has been reported to improve thermal stability [32], and to delay overaging of the Cu-added Al-alloys. The C phase on the other hand is elongated along $<001>_{\text{Al}}$, has a monoclinic unit cell, and assumes the shape of a plate [24].

QP and QC phases have been reported to be hexagonal, most likely ordered on the projected hexagonal Si-network [25]. Q' phase is similar to the B' phase, however, Cu replaces certain Al positions in this case. The Q' phase is considered to be prevalent in over-aged conditions [23], and Cu atoms may also segregate along the matrix/Q'-interfaces [33].

When the equilibrium state is reached, Q phase will be the dominating phase. There are several suggestions for the composition of the Q-phase, and a reoccurring composition is $Al_3Cu_2Mg_9Si_7$ [28]. However, density functional theory (DFT) and atom probe tomography (APT) suggest different compositions of the Q phase [34, 35], so it is likely that the composition is dependent on the alloy composition and thermomechanical treatment. An overview of the known phases in the 6xxx Al-Mg-Si-Cu system is given in Table 2.

Table 2: Precipitate phases encountered in Cu containing 6xxx Al-Mg-Si alloys [21].

Phase	Composition	Space group	Lattice parameters [nm]
L	Variable	Disordered	–
C	$Mg_4AlSi_{3.3}Cu_{0.7}$	$P2_1/m$	a = 1.032, b = 0.405, c = 0.810, $\beta = 100.9°$
QP	Unknown	Hexagonal	Likely disordered phase incorporating the Si network
QC	Unknown	Hexagonal	Likely the same as β'_{Cu} phase
Q'	$Al_3Cu_2Mg_9Si_7$	$P\bar{6}$	a = b = 1.032, c = 0.405, $\gamma = 120°$
Q	$Al_3Cu_2Mg_9Si_7$	$P\bar{6}$	a = b = 1.039, c = 0.405, $\gamma = 120°$

Another aspect to consider is how excess Si can cause formation of nano-sized Si precipitates during artificial ageing of 6xxx alloys [36, 37].

Different from the extensively studied 6xxx wrought alloys, little work has been reported with regard to the detailed characterization of the precipitation behavior of both Si precipitates and needle shaped age hardening precipitates in Al-Si-Mg based foundry alloys. This is partly due to the challenge in preparation of TEM samples of the alloys. Here we present a detailed high resolution (HR) TEM study on the precipitates formed during artificial aging treatment of A356 alloys with and without Cu. The main tools for the structural analysis is bright field and high resolution TEM, and atomic resolution 'high angle annular dark field scanning TEM' (HAADF-STEM). By using HAADF-TEM, electrons subjected to Rutherford scattering and thermal diffuse scattering can be detected. The scattering angle is proportional to the atomic number (Z), which in turn gives a higher intensity at positions corresponding to high-Z scattering centers [38, 39]. The Z-contrast in the atomic resolution HAADF-STEM images have been used to perform atomic overlays according to column arrangement principles described in [30].

2. Experimental

The experimental alloys used in this work are direct chill (DC) cast billets with a diameter of 95 mm. The melts were degassed and grain refined with an Al-Ti5-B1 master alloy. The chemical composition of the alloys are given in Table 3, as measured by x-ray fluorescence (XRF).

After casting, the alloys were solution heat treated and quenched to room temperature in water. The alloys were then heat treated in an oil bath at 175 °C for different times followed by an immediate water quenching to room temperature. An average of five hardness indentations have been used for each point in the hardness-plot showing Vickers hardness as a function of ageing time for all alloys.

Table 3: Chemical composition of the alloys in wt %.

Alloy	Si	Mg	Cu	Fe	Ti	Al
A356	7.0	0.47	0.01	0.12	0.09	Bal
A356 + 0.5 Cu	7.0	0.47	0.5	0.12	0.09	Bal
A356 + 1 Cu	7.0	0.45	1.04	0.13	0.09	Bal

Slices of 1 mm thickness were cut from the samples aged for 6 hours at 175 °C (T6 condition) and mechanically thinned to about 100 μm thickness with SiC paper. Disks of 3 mm diameters were then stamped out from the foils and electropolished in a Struers TenuPol-5. The electrolyte consisted of 2 parts methanol and 1 part nitric acid, cooled to -25 °C by adding liquid nitrogen. The TEM specimens were further ion milled to obtain a smooth surface and sufficiently thin areas for atomic resolution STEM. Ion milling was performed in a PIPSII for 30-60 minutes at 3 keV - 0.2 keV. Finally, the samples were plasma-cleaned in a Fischione plasma cleaner, model 1020, for 2 minutes in O_2/Ar plasma directly before insertion in the TEM.

The precipitate statistics presented in Table 4 are based on low magnification TEM images acquired in a JEOL 2100 operated at 200 kV. The average thickness of each imaged area was obtained using a Gatan GIF imaging filter. For a full description of the statistical approach, see [40].

A probe and image corrected JEOL ARM200F, equipped with a cold field emission gun (FEG), was used to acquire the HAADF-STEM images. An operation voltage of 200 kV was used, the probe size was 0.08 nm and the inner collector angle 50 mrad. All the precipitate cross sections have been imaged along $<100>_{Al}$.

Image stacks of 20 images were taken to minimize drift and scan distortions by use of the Smart Align software [41]. Smart Align uses a stack of images to do simple image translation, affine corrections and non-linear distortion corrections, resulting in averaged images much closer to the real lattice with respect to atomic positions and intensities. These averaged images have a much higher signal-to-noise ratio than single scans.

3. Results

3.1. Hardness evolution and microstructural overview

The hardness evolution of the three alloys is shown graphically in Figure 1. Peak hardness was reached after approximately six hours of artificial

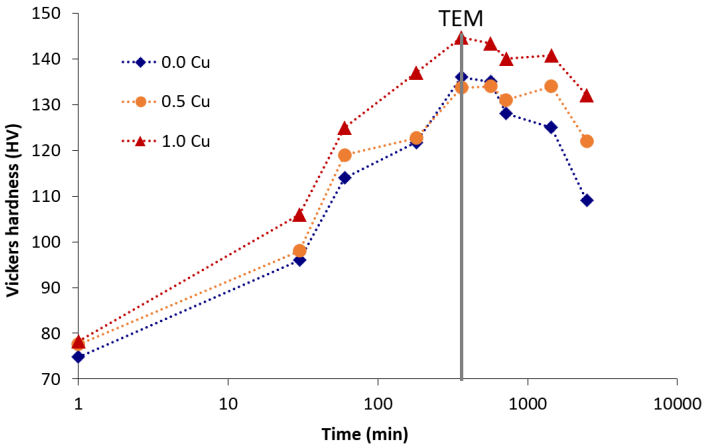

Figure 1: Vickers hardness as a function of artificial ageing time at 175°C for all alloys. TEM investigations were done after 6 hours artificial ageing, this condition is indicated by a vertical line.

ageing at 175 °C for all alloys. The six hour artificial ageing condition was selected for detailed TEM investigations, which are presented below.

From Figure 1 it can be observed that adding 1 wt% Cu to the alloy causes a significant increase in hardness at peak aged and overaged conditions. At longer ageing times, the thermal stability is improved in both the Cu-added alloys. Comparatively, the hardness values drop relatively fast in the overaged conditions for the reference alloy where no Cu was added.

The well-known eutectic silicon particles in the μm-regime were present in all the alloys. Energy dispersive X-ray spectroscopy (EDS) was performed in order to confirm that the particles consisted almost exclusively of Si. A small Al and Fe signal was detected, most likely due to the surrounding Al-matrix.

Observations of nano-particles with different morphology than the well-known needle-precipitates were observed in all alloys after ageing, see Figure 2, however in varying sizes and number densities. Atomic resolution HAADF-STEM was used to investigate these particles, an example is given in Figure 3, revealing them to consist of pure Si. The Si-precipitates were found to have an orientation relationship with the Al-matrix as follows:

$<100>_{\mathrm{Al}} \parallel <110>_{\mathrm{Si}}$ and $<010>_{\mathrm{Al}} \parallel <112>_{\mathrm{Si}}$.

Atomic columns with higher intensity along the $<112>_{\mathrm{Si}}$ precipitate-matrix interfaces are observed. The Z-contrast indicate high occupancy of Cu at these sites, with a periodicity of 1 and 1.5 Al unit cells, as indicated

by arrows. Stacking faults are present in several Si-precipitates, similar to those in Figure 3.

For alloy A356 at peak hardness (6 hours ageing) the Si-precipitates have a diameter of roughly 8 nm. After adding 0.5 wt % Cu, the Si-precipitates have grown and coarsened significantly and have an average diameter of about 50 nm. An addition of 1 wt % Cu seems to decrease the average Si particle size to about 12 nm, and the morphology changes from plate-like to spherical.

A vast majority of the hardening metastable needle precipitates nucleate homogeneously, and have the largest influence on the precipitate parameters obtained in Table 4. Some heterogeneous nucleation on dislocations was observed, but will not be discussed further here as this fraction is very low for undeformed materials. Three example TEM-micrographs corresponding to the conditions presented in Table 4 are shown in Figure 4. As can be deduced from Table 4 and by mere observation by eye, increasing the Cu-additions leads to an increase in precipitate number density, while simultaneously causing the precipitates to become smaller in length and cross section. That is, Cu-additions cause a refinement of the precipitate microstructure.

Table 4: Precipitate parameters after 6 hours ageing at 175 °C.

Alloy	Number Density [#/um^3]	Length [nm]	Cross Section [nm^2]
A356	47 500 ± 5000	18.5 ± 1.5	5.4 ± 0.4
A356 0.5 Cu	70 500 ± 7000	15.5 ± 0.5	4.3 ± 0.4
A356 1 Cu	116 000 ± 11 000	13.7 ± 1.0	3.8 ± 0.3

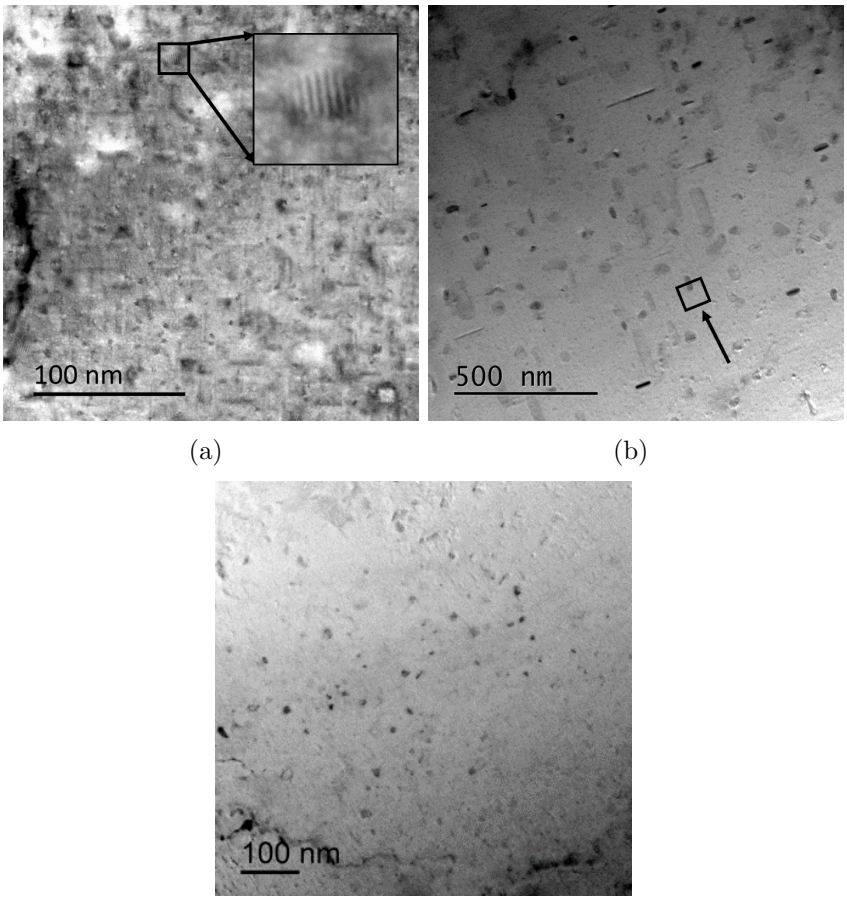

(a) (b)

(c)

Figure 2: Si precipitates after 6 hours artificial ageing in: a) A356. One Si-particle is emphasized and enlarged in the insert. b) Si particles in the A356 + 0.5 wt% Cu. The micrograph shows an area with a relatively large fraction of 'intermediate sized' Si precipitates in the foundry alloy. The arrow points out an example Si-particle similar to that imaged in Figure 3. c) A356 + 1 Cu. The Si-precipitates are mostly rounded and seem spherical in this alloy.

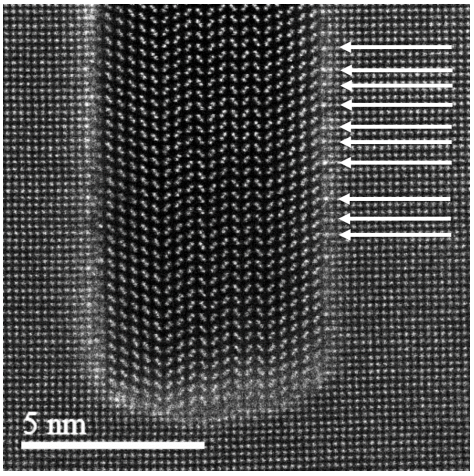

Figure 3: a) HAADF-STEM image of the marked area in Figure 2(b), showing a Si particle in A356 + 0.5 wt% Cu after 6 hours artificial ageing. The arrows point out the periodic high intensity at the precipitate/matrix-interface, most likely due to high Cu-occupancy at these atomic columns.

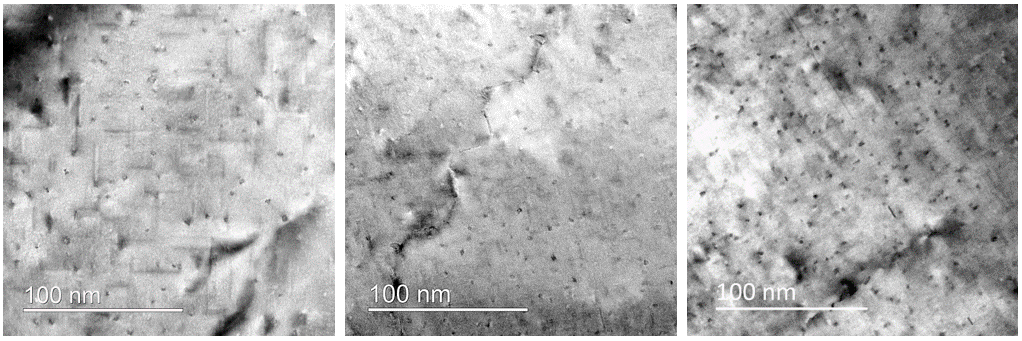

(a) (b) (c)

Figure 4: Precipitate distribution after 6 hours artificial ageing in alloy: a) A356, b) A356 + 0.5 wt% Cu and c) A356 + 1 wt% Cu. The three images are taken from areas with comparable material thicknesses.

3.2. A356 Alloy

After investigating the precipitate microstructure in alloy A356, a large majority of the cross sections were identified as β"-type. A representative TEM micrograph is given in Figure 5(a), the black arrows indicate β" cross sections. An HAADF-STEM image of a typical β" cross section from this alloy is presented in Figure 5(b). The cross section is exactly one unit cell large, see dashed lines in Figure 5(b), with unit cell vectors along <130>Al and <320>Al.

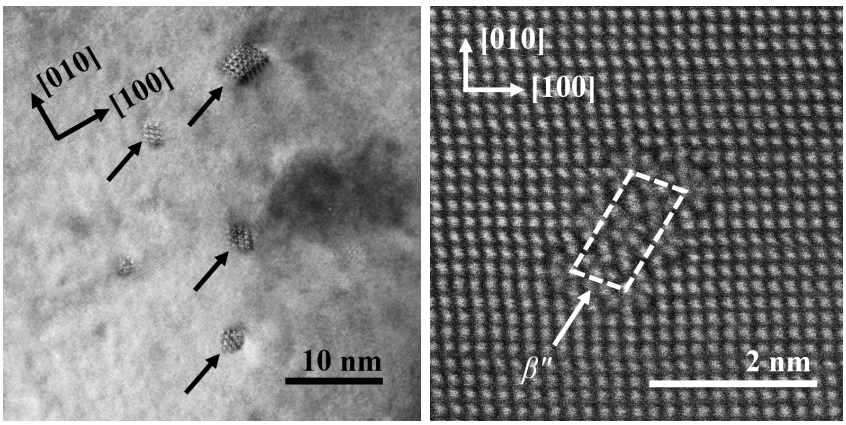

(a) (b)

Figure 5: a) TEM image from a representative area in alloy A356 after 6 hours artificial ageing. The black arrows indicate β" cross sections. b) HAADF-STEM image of a β" cross section, consisting of one unit cell. The Al crystal directions are indicated in both a) and b).

3.3. A356 with 0.5 wt% Cu

After adding 0.5 wt % Cu to the A356 alloy, atomic columns with higher contrast were detected in cross sections of most needle shaped precipitates. This strongly suggests that a majority of the cross sections contain Cu. Three HAADF-STEM images, illustrating the most commonly observed cross sections in the alloy with 0.5 wt % Cu, are given in Figure 6. Here we observe that the β" phase is still present, either alone or as sub-lattice units co-existing with sub-lattice units of other types of precipitates in the same needle cross section. However, Cu containing sub-lattice units such as Q' are here commonly co-existing with β" in the same needle precipitate, causing disorder in the latter. Some precipitates do not contain β" at all, and these were mainly determined to be L-phase.

Interestingly, in this alloy a relatively high fraction of the L-phase cross sections are observed to have an inversion center, see example in Figure 7. These cross sections have Cu-columns at the precipitate/matrix interfaces and several triangular Q'/C-plate like units, indicated by white-lined triangles in 7(b). The insert in Figure 7(b) is enlarged in Figure 7(c). This triangle illustrates the sub-lattice unit which, dependent on its stacking order, creates the disordered L-phase, or the ordered Q' or C-plate [42]. The Si atomic column in the middle of the precipitate cross section, colored in green,

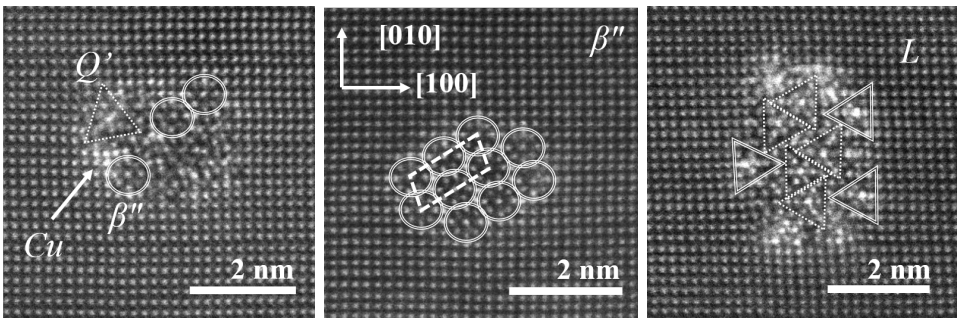

(a) (b) (c)

Figure 6: Three unprocessed HAADF-STEM images of typical precipitate cross sections in the A356 with 0.5 wt% Cu after 6 hours artificial ageing. a) Disordered precipitate cross section with Q' (triangle), and β" (circles) sub-lattice units. Cu is also observed to enrich Al matrix columns at high strain locations at the interface, as indicated by the white arrow. b) β" precipitate with stacking fault. One unit cell is indicated with dashed lines. c) L-phase precipitate containing C-plate and Q' sub-lattice units as indicated by double-lined and dashed-line triangles respectively.

Table 5: (Colour) Symbolic representation and heights of elements.

Elements / Height	Al	Si	Mg	Cu
z = 0.000 nm	○	○	○	○
z = 0.203 nm	●	●	●	●

indicates the location of the inversion center in Figure 7(b). An overview of the symbolic representation of elements is given in Table 5. The hexagonal Si network is present throughout the cross section and Cu predominately settles between the Si-network columns.

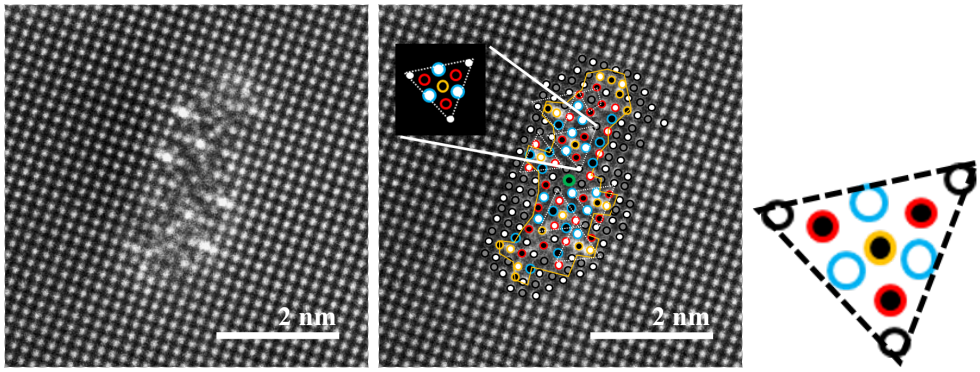

(a) (b) (c)

Figure 7: (Colour) a) HAADF-STEM 'Smart Align' average through image stack of a precipitate cross section in the A356 alloy with 0.5 wt % Cu after 6 hours artificial ageing. b) Atomic overlay of the precipitate cross section shown in a). c) Enlarged image of the insert in b) illustrating the L/C-plate sub-lattice unit. The L/C-plate sub-lattice units are indicated by white dashed lines. A symbolic representation of the elements is given in Table 5.

3.4. A356 with 1.0 wt% Cu

Alloy A356 + 1.0 wt% Cu has the highest precipitate number density in the peak aged state among the three alloys. The precipitate phases typically consist of different stacking variations of the Q'- or C-plate sub-lattice units shown in Figure 7(c), or β"-eyes. Cross sections of three precipitates are presented in Figure 8. Figure 8(a) shows an L-phase cross section and Figure 8(b) shows an overall disordered precipitate with Q' atomic-column ordering in the upper part. Based on the observed phases, the A356 + 1.0 wt% Cu alloy has similar precipitate types as A356 + 0.5 wt% Cu. However, they seem to differ with respect to the amount of Cu absorbed in the β'' phase. A β'' cross section where Cu occupies Si_3 columns is given in Figure 8(d). The Si_3 sites have a higher intensity in HAADF-STEM both at the precipitate/matrix interfaces and inside the cross section, suggesting a significant occupation of Cu atoms at these sites.

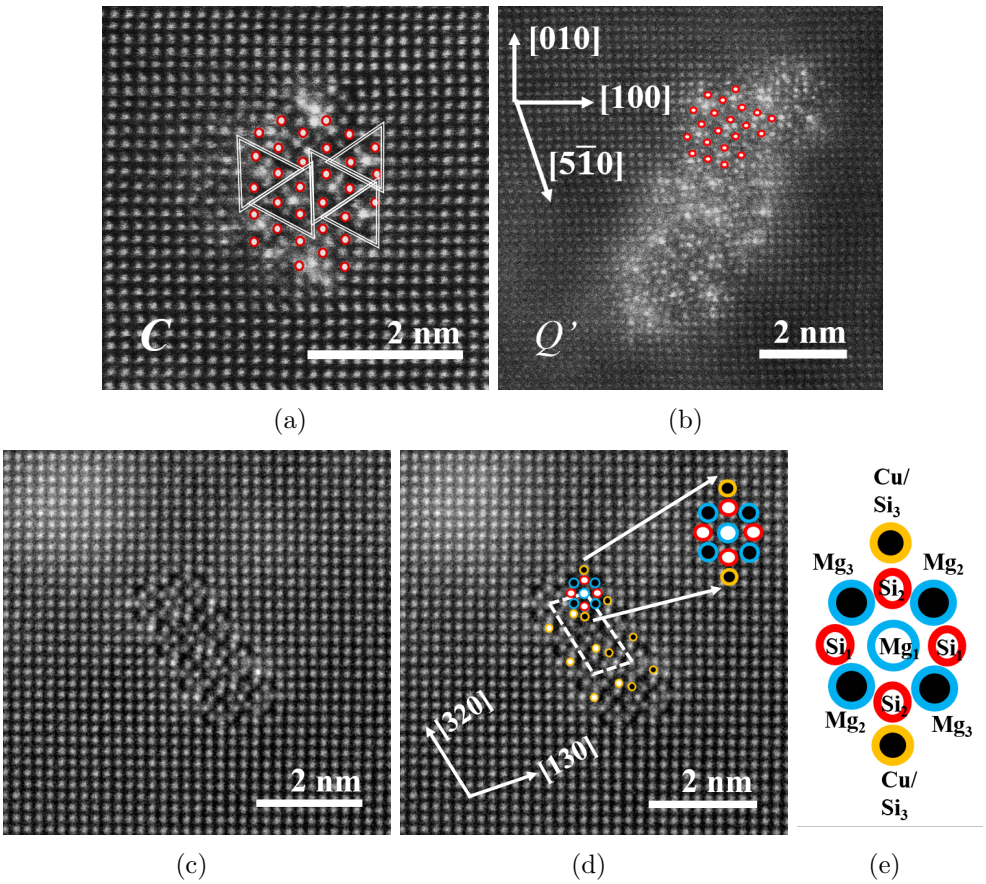

Figure 8: HAADF-STEM images of typical precipitate cross sections in A356 + 1 wt% Cu after 6 hours artificial ageing. a) Short C-phase cross section. Si columns (network), oriented along $<001>_{Al}$, are indicated by small red circles. The triangular sub-lattice units are stacked in a C-phase arrangement and are indicated by double lined triangles. b) Disordered precipitate formed on a dislocation line, with Q' arrangement in the upper part. The Si-network (indicated by red circles) is oriented along $<5\text{-}10>_{Al}$. c) β'' cross section (SmartAlign). d) The precipitate cross section from c) with partial atomic overlay. The Cu-enriched columns are indicated at Si_3-sites. One β'' unit cell is indicated with white dashed lines. e) The model of the β''-molecule in A356 + 1 Cu. All images are taken along a <001>Al zone axis, crystal directions are indicated in b) and d). A symbolic representation of the elements can be found in Table 5

4. Discussion

4.1. Si precipitates

The particles shown in Figure 2 are very similar to the Si-precipitates that form during ageing due to excess Si in 6xxx alloys [37]. Excess Si does not seem to change the precipitation sequence, but forms additional Si-nanoparticles, as shown in Figure 2. These additional Si-precipitates have previously been reported to have an insignificant contribution to material hardness [37]. According to Gupta et al., increasing Mg-content, causes the precipitation of free Si to be reduced [37]. However, it is possible that adding Cu also causes an increase in the precipitation of Si, as we see here. From density functional theory (DFT) calculations, we know that both Si and Cu bind vacancies [28, 43]. This mechanism leads to more nucleation sites for precipitation of β'', and Cu-containing Mg-Si precipitates like Q', C-plate and L. The available quenched-in vacancies are attracted to both Cu and Si solute atoms, Mg on the other hand, has a low interaction energy with vacancies, and is believed to be less involved in the nucleation process [43]. Since the amount of vacancies is the same, but the added solute with a high affinity to vacancies has increased, the precipitation of free Si should increase. Which is exactly what we observe in Figure 2.

By adding 1 wt % Cu, an apparent refinement of the Si-precipitate distribution occurs compared to 0.5 wt % Cu, see Figure 2(c). It is possible the quenched-in vacancies favor nuclei with both Si and Cu, leading to a higher number density of smaller Si-particles. The Si-precipitates are smaller because we have a constant equilibrium amount of vacancies at the ageing temperature possibly favouring solute transport to a high number of the needle-precipitate nuclei. Thus leaving less potential for the Si-particles to coarsen and grow. The precipitation of free Si does however need to be further investigated in order to get a better understanding of this behaviour.

The Si-precipitates have a periodically higher intensity in HAADF-STEM along the particle/matrix interface. Due to the absence of other high-Z elements, these periodic high intensities must be due to Cu. Previous work by Saito et al. [44] has identified Cu to suppress misfit dislocations at the interface between β" and Al in 6xxx Al-Mg-Si-Cu alloys. Due to the periodic arrangement of Cu along $<112>_{Si}$ parallel to $<010>_{Al}$, it seems Cu can also act as a misfit reliever in this context. Stacking faults along $<112>_{Si}$ in the Si-precipitates seem common, and may be necessary in order to accommodate internal stresses.

4.2. Needle Precipitates

Small differences in hardness can be seen at the beginning of ageing in Figure 1 due to solid solution hardening. At peak hardness there is a difference of about 10 HV between A356 + 1 Cu and the other two alloys. The age-hardening behavior of alloy A356 and 'A356 + 0.5 Cu' is relatively similar until peak hardness is reached, but for over-aged conditions the Cu-containing alloy has higher HV-values. The hardening effect from adding 1 wt % Cu to the alloy is attributed to the large increase in precipitate number density, shown in Table 4. It also seems that the Cu-containing precipitate phases are more stable, causing the alloy to maintain higher strength during over-ageing. When Cu is added to the alloy, the formation of β'' decreases and more L and Q' form instead. Since L and Q' are more thermally stable than β'', L and Q have a slower growth evolution. Consequently, higher numbers of smaller precipitates are preserved during over-aging, which gives higher strength to the Cu-containing alloys. It should be taken into account that further experiments with a higher artificial ageing temperature is necessary in order to conclude on the materials' potential for high-temperature applications.

Common for the two Cu-containing alloys is that both ordered and disordered precipitate structures with Cu seem to follow the Si-network rules described in [29, 30]. Cu prefers to position itself at the sites between the hexagonal Si-network columns, which is typical for L and Q'. Cu seems to only occupy Si-sites when incorporated in β'' cross sections.

Precipitate phases located on dislocation lines are identified to be larger, relative to homogeneously nucleated precipitates, these heterogeneously nucleated precipitates can also be referred to as 'over-aged phases'. This is in agreement with in-situ TEM experiments which show that heterogeneous precipitation commences earlier than homogeneous precipitation [45]. Consequently, given longer time to grow, precipitates on dislocation lines are expected to be larger with a higher fraction of "over-aged" phases. As dislocation lines act as sinks to solute atoms, such as Cu, this is in good agreement with our experimental results from HAADF-STEM.

4.2.1. A356

The main hardening precipitate phase in 'A356 + 0 Cu' is β'', as shown in Figure 5. Compared to the two respective alloys, there are no significant Z-contrast variations across the β'' -cross sections. This observation

suggest a composition of $Mg_4Si_4Al_3$ or $Mg_5Si_4Al_2$ [12, 46]. The latter composition, with Al at Si_3 sites and Mg at the Mg_1 site, have been deemed most favourable to form when comparing the calculated formation enthalpy of different precipitates [47].

4.2.2. A356 + 0.5 wt% Cu

By adding 0.5 wt % Cu, the precipitate number density increases. This is partly due to a higher level of solute available for precipitation, consequently leading to a higher number density of precipitates. Secondly, Cu is reported to accelerate the age hardening response during artificial ageing [48]. This effect has earlier been explained by the ability of Cu to slightly reduce the solubility of Si and Mg in solid solution [49], in addition to Cu's relatively high affinity to vacancies [43].

The precipitate number densities and sizes calculated for 'A356 + 0 Cu' and 'A356 + 0.5 Cu' result in similar HV values around peak hardness. There are examples in literature where low number densities of relatively large precipitate needles result in the same material hardness as higher number densities of small needles [50]. This illustrates that the total length of precipitates available to impede dislocation motion should be considered, and not only number densities alone. When 'A356 + 0 Cu' and 'A356 + 0.5 Cu' are further artificially aged, the Cu-free alloy overages more rapidly than the Cu-added alloy. This is due to the slower precipitate growth and coarsening of phases incorporating Cu. Simultaneously, it is very likely the precipitates in 'A356 + 0 Cu' overage relatively quickly, becoming large and coarsely distributed.

Precipitates with cross sections like those presented in Figure 6 and Figure 7 appear frequently in the 0.5 % Cu alloy, and the high intensity columns show that Cu is contained in the precipitate structures. The recurring phases are Q', short C-plate or L and β''. It is frequently observed that one precipitate can contain several fragments of different precipitate phases, as shown in Figure 6(a). However in this case, a large part of the cross sections seem to consist of single phases, see Figure 6(b) and 6(c).

L-phase is recognized by the alignment of the Si-network along $<100>_{Al}$ throughout the precipitate cross section. This phase is closely related to C-plate, but the increased disorder causes the 0.81 nm periodicity to be broken, thus growth in the $<100>_{Al}$ direction is limited and the precipitates remain short instead of becoming plates [23, 32].

The L-phase occurs frequently in this alloy, and often contains an inver-

sion center at the Si-columns in the center of the cross section, with half of the cross section shifted one $\{200\}_{Al}$ plane, perpendicular to the viewed plane. The inversion center seems common, and an example is shown in Figure 7 with the inversion center column marked in green. Cu columns appear between the projected hexagonal Si-network columns and at the precipitate/matrix interfaces. Such behavior suggest that nucleation of the needle may have commenced at, or close to, the Si-column located in the inversion center. DFT calculations in previous studies have shown that Cu indeed has a high affinity to both vacancies and Si in Al [43].

4.2.3. A356 + 1 wt% Cu

When 1 wt % Cu is added to the alloy, further increase in hardness and precipitate number density is achieved. This behavior has also been reported by Li et al., however focusing more on material strength [2]. In this alloy, the β''-phase occurs less frequently than in the two alloys discussed above, and a higher fraction of Q' and L-phases is observed.

After performing SmartAlign on an image stack of 20 frames on a β'' cross section, it was revealed that the intensities at Si_3-sites were consistently higher than the other Si-sites throughout the cross section. In Figure 8(d), the β'' cross section is shown with a partial atomic overlay. This behavior has been reported for Si_3-sites at the precipitate/matrix interface in 6xxx-alloys, and in some cases for the Si_3-sites inside the cross section [42, 44, 51–53]. It has been speculated if this effect is dependent on the size of the cross section, however DFT calculations deem it energetically favorable for Cu to occupy Si_3-sites throughout the cross sections [42], which is in agreement with the experimental results here.

5. Conclusive remarks

Nanosized Si particles were discovered to precipitate in all the three alloys during artificial aging due to excess Si in solid solution. The Si-precipitates were found to have an orientation relationship to Al as: $<100>_{Al} \parallel <110>_{Si}$, and $<010>_{Al} \parallel <112>_{Si}$.

Adding Cu to the A356 foundry alloys caused an increase in the material peak hardness during artificial aging and improved the thermal stability for over-aged conditions. The enhanced age hardening behavior was attributed to a significant increase in the number density of the metastable precipitate

needles, while the improved thermal stability was due to the precipitation of more thermally stable Cu-containing precipitates.

After a peak hardness aging treatment, the precipitates in alloy A356 are dominated by the needle shaped β'' phase. When 0.5 wt% Cu was added, a large fraction of L-phase and Q' precipitates were formed in addition to the β'' precipitates. By adding 1 wt% Cu, the precipitate number density was much increased in comparison to the A356 base alloy, while L and Q'-phase became the dominant precipitates. Most of the precipitates were found to have disordered crystal structures in the cross section, containing fragments of different precipitate phases co-existing in the same needle. Some perfect β'' precipitates were still observed after 1 wt% Cu was added, where Cu atoms were identified to occupy the Si_3-sites in the cross sections. A large fraction of the L-phase precipitates were found to contain an inversion center, predominantly at a Si-column in their centers.

Acknowledgments

The (S)TEM work was carried out on the NORTEM infrastructure (NFR197405) at the TEM Gemini Centre, Norwegian University of Science and Technology (NTNU), Norway.

References

[1] R. Li, R. Li, Y. Zhao, L. He, C. Li, H. Guan, Z. Hu, Age-hardening behavior of cast Al–Si base alloy, Materials Letters 58 (2004) 2096 – 2101.

[2] Y. Li, S. Brusethaug, A. Olsen, Influence of Cu on the mechanical properties and precipitation behavior of AlSi7Mg0.5 alloy during aging treatment, Scripta Materialia 54 (2006) 99 – 103.

[3] R. Mahmudi, P. Sepehrband, H. Ghasemi, Improved properties of A319 aluminum casting alloy modified with Zr, Materials Letters 60 (2006) 2606 – 2610.

[4] Y. Xing, Z. Jia, J. Li, L. Ding, H. Huang, Q. Liu, Microstructure and mechanical properties of foundry Al–Si–Cu–Hf alloy, Materials Science and Engineering: A 722 (2018) 197 – 205.

[5] G. A. Edwards, K. Stiller, G. L. Dunlop, M. J. Couper, The composition of fine-scale precipitates in Al–Mg–Si alloys, Mater. Sci. Forum 217–222 (1996) 713–718.

[6] K. Matsuda, Y. Sakaguchi, Y. Miyata, Y. Uetani, T. Sato, A. Kamio, S. Ikeno, Precipitation sequence of various kinds of metastable phases in Al–1.0mass% Mg_2Si–0.4mass% Si alloy, J. Mater. Sci. 35 (2000) 179–189.

[7] M. Murayama, K. Hono, Pre-precipitate clusters and precipitation processes in Al–Mg–Si alloys, Acta Mater. 47 (1999) 1537–1548.

[8] A. Serizawa, S. Hirosawa, T. Sato, Three-dimensional atom probe characterization of nanoclusters responsible for multistep aging behavior of an Al–Mg–Si alloy, Met. Mater. Trans. A 39 (2008) 243–251.

[9] M. Torsæter, H. S. Hasting, W. Lefebvre, C. D. Marioara, J. C. Walmsley, S. J. Andersen, R. Holmestad, The influence of composition and natural aging on clustering during preaging in Al–Mg–Si alloys, J. Appl. Phys. 108 (2010) 073527.

[10] C. D. Marioara, S. J. Andersen, J. Jansen, H. W. Zandbergen, Atomic model for GP-zones in a 6082 Al–Mg–Si system, Acta Materialia 49 (2001) 321–328.

[11] H. W. Zandbergen, S. J. Andersen, J. Jansen, Structure determination of Mg5Si6 particles in Al by dynamic electron diffraction studies, Science 277 (1997) 1221–1225.

[12] H. S. Hasting, A. G. Frøseth, S. J. Andersen, R. Vissers, J. C. Walmsley, C. D. Marioara, F. Danoix, W. Lefebvre, R. Holmestad, Composition of β'' precipitates in Al–Mg–Si alloys by atom probe tomography and first principles calculations, J. Appl. Phys. 106 (2009) 123527.

[13] C. Cayron, P. A. Buffat, Transmission electron microscopy study of the β' phase (Al–Mg–Si alloys) and QC phase (Al–Cu–Mg–Si alloys): ordering mechanism and crystallographic structure, Acta Materialia 48 (2000) 2639 – 2653.

[14] R. Vissers, M. A. van Huis, J. Jansen, H. W. Zandbergen, C. D. Marioara, S. J. Andersen, The crystal structure of the β' phase in Al–Mg–Si alloys, Acta Materialia 55 (2007) 3815–3823.

[15] S. Andersen, C. Marioara, R. Vissers, A. Frøseth, H. Zandbergen, The structural relation between precipitates in Al–Mg–Si alloys, the Al-matrix and diamond silicon, with emphasis on the trigonal phase U1–MgAl2Si2, Materials Science and Engineering: A 444 (2007) 157 – 169.

[16] S. J. Andersen, C. D. Marioara, A. Frøseth, R. Vissers, H. W. Zandbergen, Crystal structure of the orthorhombic U2–$Al_4Mg_4Si_4$ precipitate in the Al–Mg–Si alloy system and its relation to the β' and β'' phases, Mater. Sci. Eng. A 390 (2005) 127 – 138.

[17] R. Vissers, C. D. Marioara, S. J. Andersen, R. Holmestad, Crystal structure determination of the β' phase in Al–Mg–Si alloys by combining quantitative electron diffraction and ab initio calculations, in: Proceedings of ICAA11, volume Vol. 2, pp. 1263 – 1269. ISBN 9978-3-527-32367-8.

[18] N. A. Bul'enkov, A. G. Yakovenko, O. M. Ul'yanikhina, X-ray diffraction study of the Mg2Si–Mg2Ge system, Journal of Structural Chemistry 11 (1971) 1059–1061.

[19] M. H. Jacobs, The structure of the metastable precipitates formed during ageing of an Al–Mg–Si alloy, Philosophical Magazine 26 (1972) 1–13.

[20] C. D. Marioara, S. J. Andersen, A. Birkeland, R. Holmestad, Orientation of silicon particles in a binary Al–Si alloy, J. Mater. Sci. 43 (2008) 4962–4971.

[21] T. Saito, E. A. Mørtsell, S. Wenner, C. D. Marioara, S. J. Andersen, J. Friis, K. Matsuda, R. Holmestad, Atomic structures of precipitates in Al–Mg–Si alloys with small additions of other elements, Advanced Engineering Materials 20 (2018) 1800125.

[22] D. Chakrabarti, D. E. Laughlin, Phase relations and precipitation in Al–Mg–Si alloys with Cu additions, Progress in Materials Science 49 (2004) 389 – 410.

[23] C. D. Marioara, S. J. Andersen, T. N. Stene, H. Hasting, J. Walmsley, A. T. J. Van Helvoort, R. Holmestad, The effect of Cu on precipitation in Al–Mg–Si alloys, Phil. Mag. 87 (2007) 3385–3413.

[24] M. Torsæter, F. J. H. Ehlers, C. D. Marioara, S. J. Andersen, R. Holmestad, Applying precipitate-host lattice coherency for compositional determination of precipitates in Al–Mg–Si–Cu alloys, Phil. Mag. 92 (2012) 3833–3856.

[25] C. Cayron, L. Sagalowicz, O. Beffort, P. A. Buffat, Structural phase transition in Al–Cu–Mg–Si alloys by transmission electron microscopy study on an Al–4 wt% Cu–1 wt% Mg–Ag alloy reinforced by SiC particles, Philosophical Magazine A 79 (1999) 2833–2851.

[26] K. Matsuda, S. Ikeno, Y. Uetani, T. Sato, Metastable phases in an Al–Mg–Si alloy containing copper, Metallurgical and Materials Transactions A 32 (2001) 1293–1299.

[27] L. Arnberg, B. Aurivillius, The crystal structure of Al(x)Cu2Mg(12-x)Si7, h-AlCuMgSi, Acta Chem. Scand. 34A (1980) 1–5.

[28] C. Wolverton, Crystal structure and stability of complex precipitate phases in Al–Cu–Mg–(Si) and Al–Zn–Mg alloys, Acta Materialia 49 (2001) 3129 – 3142.

[29] F. J. H. Ehlers, S. Wenner, S. J. Andersen, C. D. Marioara, W. Lefebvre, C. B. Boothroyd, R. Holmestad, Phase stabilization principle and precipitate-host lattice influences for Al–Mg–Si–Cu alloy precipitates, Journal of Materials Science 49 (2014) 6413–6426.

[30] S. J. Andersen, C. D. Marioara, J. Friis, R. Bjørge, Q. Du, I. Ringdalen, S. Wenner, , E. A. Mørtsell, R. Holmestad, T. Saito, J. Røyset, O. Reiso, Directionality and column arrangement principles of precipitates in Al–Mg–Si–(Cu) and Al–Mg–Cu linked to line defect in Al, in: The 15th International Conference on Aluminium Alloys, volume 877 of *Materials Science Forum*, Trans Tech Publications, 2017, pp. 461–470.

[31] M. Torsæter, W. Lefebvre, C. D. Marioara, S. J. Andersen, J. C. Walmsley, R. Holmestad, Study of intergrown L and Q' precipitates in Al–Mg–Si–Cu alloys, Scripta Materialia 64 (2011) 817 – 820.

[32] C. D. Marioara, S. J. Andersen, J. Røyset, O. Reiso, S. Gulbrandsen-Dahl, T.-E. Nicolaisen, I.-E. Opheim, J. F. Helgaker, R. Holmestad, Improving thermal stability in Cu-containing Al–Mg–Si alloys by precipitate optimization, Metallurgical and Materials Transactions A 45 (2014) 2938–2949.

[33] K. Matsuda, D. Teguri, Y. Uetani, T. Sato, S. Ikeno, Cu-segregation at the Q'/α-Al interface in Al–Mg–Si–Cu alloy, Scripta Materialia 47 (2002) 833 – 837.

[34] A. Biswas, D. J. Siegel, D. N. Seidman, Compositional evolution of Q-phase precipitates in an aluminum alloy, Acta Materialia 75 (2014) 322 – 336.

[35] A. Bobel, K. Kim, C. Wolverton, M. Walker, G. B. Olson, Equilibrium composition variation of Q-phase precipitates in aluminum alloys, Acta Materialia 138 (2017) 150 – 160.

[36] A. Gupta, D. LLoyd, Study of precipitation kinetics in a super purity Al–0.8 pct Mg–0.9 pct Si alloy using differential scanning calorimetry, Met. Mater. Trans. A 30 (1999) 879–890.

[37] A. Gupta, D. Lloyd, S. Court, Precipitation hardening in Al–Mg–Si alloys with and without excess Si, Materials Science and Engineering: A 316 (2001) 11 – 17.

[38] T. Yamazaki, M. Kawasaki, K. Watanabe, I. Hashimoto, M. Shiojiri, Effect of small crystal tilt on atomic-resolution high-angle annular dark field STEM imaging, Ultramicroscopy 92 (2002) 181 – 189.

[39] P. Nellist, S. Pennycook, Incoherent imaging using dynamically scattered coherent electrons, Ultramicroscopy 78 (1999) 111 – 124.

[40] C. D. Marioara, S. J. Andersen, H. Zandbergen, R. Holmestad, The influence of alloy composition on precipitates of the Al–Mg–Si system, Metallurgical and Materials Transactions A 36 (2005) 691–702. 10.1007/s11661-005-0185-1.

[41] L. Jones, H. Yang, T. J. Pennycook, M. S. J. Marshall, S. Van Aert, N. D. Browning, M. R. Castell, P. D. Nellist, Smart align—a new tool

for robust non-rigid registration of scanning microscope data, Advanced Structural and Chemical Imaging 1 (2015) 8.

[42] T. Saito, C. D. Marioara, S. J. Andersen, W. Lefebvre, R. Holmestad, Aberration-corrected HAADF-STEM investigations of precipitate structures in Al–Mg–Si alloys with low Cu additions, Philosophical Magazine 94 (2014) 520–531.

[43] E. A. Mørtsell, S. J. Andersen, J. Friis, C. D. Marioara, R. Holmestad, Atomistic details of precipitates in lean Al-Mg-Si alloys with trace additions of Ag and Ge studied by HAADF-STEM and DFT, Philosophical Magazine 97 (2017) 851–866.

[44] T. Saito, F. J. Ehlers, W. Lefebvre, D. Hernandez-Maldonado, R. Bjørge, C. D. Marioara, S. J. Andersen, E. A. Mørtsell, R. Holmestad, Cu atoms suppress misfit dislocations at the β"/Al interface in Al–Mg–Si alloys, Scripta Materialia 110 (2016) 6–9.

[45] S. K. Malladi, Q. Xu, M. A. van Huis, F. D. Tichelaar, K. J. Batenburg, E. Ycelen, B. Dubiel, A. Czyrska-Filemonowicz, H. W. Zandbergen, Real-time atomic scale imaging of nanostructural evolution in aluminum alloys, Nano Letters 14 (2014) 384–389. PMID: 24329182.

[46] S. Andersen, H. Zandbergen, J. Jansen, C. Trholt, U. Tundal, O. Reiso, The crystal structure of the β" phase in Al–Mg–Si alloys, Acta Materialia 46 (1998) 3283 – 3298.

[47] E. A. Mørtsell, C. D. Marioara, S. J. Andersen, I. G. Ringdalen, J. Friis, S. Wenner, J. Ryset, O. Reiso, R. Holmestad, The effects and behaviour of Li and Cu alloying agents in lean Al–Mg–Si alloys, Journal of Alloys and Compounds 699 (2017) 235 – 242.

[48] W. F. Miao, D. E. Laughlin, Effects of Cu content and preaging on precipitation characteristics in aluminum alloy 6022, Metallurgical and Materials Transactions A 31 (2000) 361–371.

[49] D. Collins, Constitutional factors affecting the tensile properties of wrought aluminium-magnesium-silicon-copper alloys, J. Inst. Metals 86 (1958).

[50] E. A. Mørtsell, C. D. Marioara, S. J. Andersen, J. Røyset, O. Reiso, R. Holmestad, Effects of germanium, copper, and silver substitutions on hardness and microstructure in lean Al–Mg–Si alloys, Metallurgical and Materials Transactions A 46 (2015) 4369–4379.

[51] T. Saito, S. Wenner, E. Osmundsen, C. D. Marioara, S. J. Andersen, J. Røyset, W. Lefebvre, R. Holmestad, The effect of Zn on precipitation in Al–Mg–Si alloys, Philosophical Magazine 94 (2014) 2410–2425.

[52] K. Li, A. Beche, M. Song, G. Sha, X. Lu, K. Zhang, Y. Du, S. P. Ringer, D. Schryvers, Atomistic structure of Cu-containing β" precipitates in an Al–Mg–Si–Cu alloy, Scripta Materialia 75 (2014) 86 – 89.

[53] L. Ding, Z. Jia, J.-F. Nie, Y. Weng, L. Cao, H. Chen, X. Wu, Q. Liu, The structural and compositional evolution of precipitates in Al–Mg–Si–Cu alloy, Acta Materialia 145 (2018) 437 – 450.